Efficient nano-regional photocatalytic heterostructure design *via* the manipulation of reaction site self-quenching effect

Han Feng[a,1], Liangliang Liang[b,1], Yu Liu[a,d], Zhaohong Huang[c], Lin Li[e,*]

[a] *Advanced Environmental Biotechnology Centre, Nanyang Environment and Water Research Institute, Nanyang Technological University, 1 Cleantech Loop, Singapore 637141, Singapore*
[b] *Department of chemistry, National University of Singapore, Science Drive 3, Singapore 117543, Singapore*
[c] *Singapore Institute of Manufacturing Technology, Fusionopolis Way, Innovis, Singapore 138634, Singapore*
[d] *School of Civil and Environmental Engineering, Nanyang Technological University, Singapore 639798, Singapore*
[e] *School of Mechanical and Aerospace Engineering, Nanyang Technological University, 50 Nanyang Avenue, Singapore 639798, Singapore*

ARTICLE INFO

ABSTRACT

Heterostructural photocatalysts with rationally aligned energy bands have been proved effective in diminishing the recombination of photo-induced excitons, thus leading to enhanced photocatalytic performance. However, the critical role of charge carrier behaviors and their quenching pathway in determining the overall photocatalytic performance are still not fully explored, which severely hindered the development for efficient photocatalysts. Herein, to further explore the essential principles of photocatalysis with heterostructures, a representative nano-regional photocatalytic heterostructure was constructed through uniform decoration of visible light activable BiOI nanodots on TiO_2 nanorod assembled microflowers. With which as a well-known prototype of conventional heterostructures, a possible photocatalytic performance annihilation channel *via* reaction site self-quenching effect in photocatalytic heterostructures was experimentally evidenced for the first time. Based on our experimental results, we evidenced that excessive decoration with BiOI nanodots would result in severe self-quenching of their photocatalytic sites through highly probable charge carrier recombination between migrating electrons along TiO_2 nanorods and reactive holes in adjacent BiOI nanodots. Such fundamental and experimental discovery is not limited to the current model and would shed light on the development of novel nano-regional heterostructures with high photocatalysis performance.

1. Introduction

Heterostructures with rationally designed junction have long been extensively studied and applied in many emerging applications ranging from solar cells [1–7], photodetectors [8–10] to photo/electro-catalysis [11–15]. Especially in the development of high-performance photocatalysts for clean energy generation [16–19] or pollutant clearance [12,13,20,21], heterostructures constructed with different semiconductor [22] (or metal [23,24]) components are much preferred owing to their programmable optical and electrical advances such as the wide spectral response which can even reach the near-infrared (NIR) region [25,26] and effective separation of photoinduced excitons for prolonged lifetime of reactive sites [27,28]. Therefore, in the past several decades, photocatalytic heterostructures have received extensive attention, and significant progress has been made in developing outstanding photocatalytic platforms and understanding the

mechanism of photocatalysis in nanoscale.

In a conventional semiconductor-mediated photocatalytic heterostructure, two or more components with suitable energy band configurations are physically or chemically combined to build charge carrier diffusion channels driven by the potential difference [29]. Benefiting from this, photoinduced excitons could be effectively separated through the interfacial carrier diffusion, resulting in profoundly mitigated reactive site loss and significantly enhanced catalytic performance. Generally, to ensure highly efficient charge carrier separation and shorten its transportation distance, decoration of one nanosized semiconductor component onto another nano- or micron-sized one is highly desired. Recently, various photocatalytic heterostructures such as Ag_2O nanoparticles attached on the surface of TiO_2 microspheres ($TiO_2@Ag_2O$) [30], quantum dots decorated g-C_3N_4 sheets ($C_3N_4@QDs$) [31], and carbon nanodots modified BiOI microspheres (BiOI@CDs) [32] were developed. Besides the enhanced photocatalytic performance with

---

these heterostructures, all these works observed a performance decrease when the amount of nano-decorators exceed a critical value. Although some researchers inferred that excessive nano-decorators would lead to an increased light penetration depth in the space charge layer [30,33,34] or reaction site blocking [12,31,32] in these heterostructures, these explanations are left unverified by experimental result, and the mechanism behind the concentration vanishment of photocatalytic performance is still in controversy. As a result, there may be some omitted channels for the annihilation of photocatalytic performance in the nano-regional heterostructures, which should be further explored.

In this work, a novel nano-regional photocatalytic heterostructure was constructed through decorating p-type BiOI nanodots onto the surface of n-type TiO$_2$ nanorod assembled microflowers, forming a suitable type-II [35] band alignment by p-n junction. Generally, micron-sized BiOI sheets are usually obtained due to their intrinsic fast crystal growth [36–38] through conventional synthesis strategies, such as electrodeposition [36] and chemical bath method [39,40]. Herein, by means of a reactant pre-fixing strategy, for the first time, we successfully prepared extremely small (< 3 nm) and uniform BiOI nanodots on the surface of TiO$_2$ nanorods. In this heterostructure, BiOI nanodots are highly responsive to visible light stimulation, and photoinduced electrons could transfer efficiently from these nanodots to bulky TiO$_2$ nanorods benefiting from the ultrasmall size of BiOI nanodots and strong interfacial bonding with their TiO$_2$ counterparts [21,41]. The photodegradation study based on Rhodamine B confirmed the significant photocatalytic performance improvement induced by the heterostructure design, and a catalytic performance annihilation effect was observed when excessive BiOI nanodots were decorated. Based on the experimental investigation, we proposed that the excessive decoration of the BiOI nanodots may trigger a photocatalytic site self-quenching effect which could be a possible channel responsible for the sacrificed photocatalytic capability, and it was further evidenced by time-resolved fluorescence decay study. We believe the photocatalytic site self-quenching effect could be extended to other nano-regional photocatalytic heterostructures and pave the way for high-performance heterostructure design in many emerging applications.

2. Experimental section

2.1. Materials

Titanium (IV) butoxide (TBT, Ti(OCH$_2$CH$_2$CH$_2$CH$_3$)$_4$, 98%), hydrochloric acid (HCl, about 37% by weight), oleic acid (OA, C$_{18}$H$_{34}$O$_2$), bismuth iodide (BiI$_3$), absolute ethanol, rhodamine B (RhB, C$_{28}$H$_{32}$C$_1$N$_2$O$_3$), isopropanol, potassium peroxydisulfate (K$_2$S$_2$O$_8$), ethylenediaminetetra acetic acid disodium (EDTA-2Na), and phenol (C$_6$H$_6$O) were purchased from Sigma-Aldrich Co. Ltd. All the chemicals were used as received without further treatment.

2.2. Preparation of nano-regional heterostructures

For the preparation of nano-regional heterostructure, TiO$_2$ nanorod assembled microflowers were firstly synthesized, followed by the decoration of BiOI nanodots on the former. A hydrothermal method reported in a previously published work was adopted for the synthesis of TiO$_2$ microflowers [42]. Briefly, a mixture of 4 mL titanium butoxide and 1.85 mL concentrated HCl was added into 20 mL oleic acid slowly under continuous magnetic stirring. After stirring for about 15 min, the solution was transferred into a Teflon lined autoclave with a capacity of 45 mL. The hydrothermal process was conducted at 180 °C for 4 h and then naturally cooled down to room temperature (RT). The as-received product was washed with DI water and ethanol for several times and then dried at 80 °C for 12 h to get TiO$_2$ microflowers. Finally, a calcination process was conducted at 450 °C for 1 h to improve the crystallinity of prepared samples.

The nano-regional heterostructure constructed with BiOI nanodots and TiO$_2$ microflowers was synthesized by a novel reactant pre-fixing method. 10 mL of absolute ethanol dispersed with different amount (0.5 mg, 1 mg, 2 mg, and 4 mg) of BiI$_3$ was added into 10 mL absolute ethanol dispersed with 100 mg of TiO$_2$ microflowers. The mixture was firstly stirred vigorously at RT for 3 h and then under 80 °C until the ethanol was fully evaporated to become brown powder. After that, the obtained powder was redissolved in 50 mL DI water and kept stirred at 80 °C for 5 h. Finally, the product was washed with ethanol and DI water in sequence for about 4–5 times and then dried at 80 °C for 5 h. The as-prepared samples were labeled as TiO$_2$@BiOI (X%), where X% stands for the weight ratio of BiI$_3$ and TiO$_2$ microflowers used in the reaction (X = 0.5, 1, 2, and 4). Pure BiOI without TiO$_2$ microflowers was also synthesized using the same method.

2.3. Characterization

The crystal structure of the as-prepared heterostructures was examined by X-ray diffraction (XRD, D8, Advanced, Bruker). The XRD patterns were recorded with Cu-Kα radiation (λ = 1.5406 Å) from 10° to 80° at a scanning speed of 1.03° min^{-1} with the X-ray tube voltage and current of 40 kV and 30 mA, respectively. Field emission scanning electron microscopy (FE-SEM, JEOL-7660F), energy dispersive X-ray spectroscopy (EDS, Oxford Xmax80 LN2 Free), and high-resolution transmission electron microscopy (TEM/HRTEM, JEOL-1400) were used to get the size, morphological and lattice structural information of the prepared heterostructures. The elemental compositions and chemical status were analyzed by X-ray photoelectron spectroscopy (XPS, HSA-3500, SPECS, Germany). The specific surface area was measured by N$_2$ adsorption-desorption using the Brunauer–Emmett–Teller (BET, Micromeritics ASAP2020) method. Inductively coupled plasma optical emission spectrometry (ICP-OES, Thermo Fisher) was conducted to test the real composition of the synthesized heterostructures. UV–vis diffuse reflectance spectra (DRS, Perkin-Elmer Lambda 1050) were measured with the prepared powder samples over the wavelength range from 350 nm to 700 nm. Electrochemical impedance spectroscopy (EIS) was examined on a BioLogic VSP 300 potentiostat/galvanostat device. The measurements were conducted in a classic three-electrode cell using the photocatalysts, Pt wire and Ag/AgCl as working, counter, and reference electrodes, respectively, and 0.5 M Na$_2$SO$_4$ aqueous solution was used as the electrolyte. The working electrodes were prepared by uniformly dispersing the mixture of 20 mg photocatalyst and 100 μL Nafion and 1.9 mL isopropanol to the FTO surface [43] with the area of 1 cm^2. Then the as-prepared electrodes were dried in air under 80 °C. The EIS measurements were carried out between 100 kHz and 10 MHz. Photographic images of prepared powers were taken with a Canon camera.

The fluorescence lifetime measurement was performed under excitation of 420 nm femtosecond pulses. The light source used was a mode-locked Ti: sapphire laser (Chameleon Ultra II, Coherent) working at a repetition rate of 80 MHz and a pulse duration of 140 fs, and the luminescence decay at 550 nm was recorded. For the simulation of fluorescence decay, a biexponential decay model as below was used and intensity contribution and lifetime of each stage were extracted from simulated results.

$$I_t = I_1 e^{-\frac{t}{\tau_1}} + I_2 e^{-\frac{t}{\tau_2}}$$

Where I_t is the fluorescence intensity at time of t, I_1 and I_2 is the fluorescence contribution of stage 1 and stage 2, respectively. τ_1 and τ_2 is the fluorescence decay lifetime of stage 1 and stage 2, respectively.

2.4. Measurement of catalytic properties

Photocatalytic degradation experiments were carried out in a quartz reactor using Rhodamine B as the model organic pollutant under simulated solar light (SAN-EI ELECTRIC CO., XES-151S). In a typical run,

before irradiation, a mixture of 50 mg as-prepared photocatalyst and 50 mL 1×10^{-5} M RhB was stirred in the dark for 1 h to get adsorption-desorption equilibrium. During the irradiation process ($100 \, mW/cm^2$), the mixture was kept stirring and 2 mL of the solution was taken out every 15 min and centrifuged to analyze the residue pollutant concentration using UV–vis spectrometer (Perkin-Elmer Lambda 1050) at the wavelength of 554 nm [44]. The degradation intermediates were detected by GC–MS (GCMSQP2010ULTRA, Shimadzu, Japan) equipped with Rtx-5MS column to investigate the photodegradation pathway of RhB. The degree of photo mineralization of RhB was measured using a TOC/TN analyzer (Shimazu) connected to an auto-sampler (TOCLCSH/CSN Model, Shimadzu Co., Kyoto, Japan). As a comparison, the photocatalytic activity of pure TiO_2 microspheres was also examined using the same conditions. In addition, for each sample, a 420 nm long pass filter (FGL 420, Thorlabs) and a UV bandpass filter (FGUV5, Thorlabs) were alternatively used to simulate the situation of Visible and UV light-mediated photocatalysis.

To explore the predominant reactive species in this photocatalytic process, we choose isopropanol (IPA), potassium peroxydisulfate ($K_2S_2O_8$) and Ethylenediaminetetra acetic acid disodium (EDTA-2Na) as hydroxyl radical, electron, and hole scavengers, respectively. In each typical run, 1 mM of the scavengers were added to the mixture of 50 mL 10 mg/L RhB and TiO_2@BiOI (2%) and then irradiated under solar light.

Since RhB is photo-sensitive, colorless phenol was used as another organic pollutant to further confirm the photocatalytic ability of our synthesized heterostructures. Typically, 50 mg catalysts were dispersed into 50 mL of 10 mg/L phenol aqueous solution, and the mixture was kept stirring in the dark for an hour to get adsorption-desorption equilibrium. Full spectrum solar light was used as energy source and 2 mL of the solution was taken out every 15 min and centrifuged to analyze the residue phenol concentration using high-performance liquid chromatography (HPLC, Shimadzu LC system (LC-20AD)) equipped with an SB-C18 (4.6 × 150 mm) column. The mobile phase used was a mixture of methanol and water (70/30 by volume) at a flow rate of 1.0 mL/min with an analytical wavelength of 270 nm.

3. Results and discussion

As shown in Fig. 1a, in our design, to build a universal nano-regional visible light responsive photocatalytic heterostructure model, a platform with p-type visible light sensitive nanodots attached on the surface of a bulky n-type substrate was intended to be constructed. In this platform, photocatalytic sites were designed to locate on these nanodots to eliminate the photocatalytic site blocking effect induced by heavy loading [12]. Upon visible light illumination, photoinduced electrons from nanodots could drift across the crystal interface and

diffuse along the substrate, while holes are left in the valence band of nanodots to trigger the photocatalytic oxidation reaction. Advanced with the efficient exciton separation and smooth electron diffusion channel along the substrate, we can anticipate a high photocatalytic performance with this model. In addition, the amount of nanodots decorated on the surface of bulky substrate could be easily tuned in a wide range, which would provide us a chance to study the evolution of catalytic performance along with the amount variation of decorated nanodots (Fig. 1b). Based on these design principles, as illustrated in Fig. 1c, we constructed a photocatalytic heterostructure with TiO_2 nanorod assembled microflowers as the n-type substrate for electron migration and BiOI nanodots as the p-type visible light responsive nano-decorators to create the nano-regional photocatalytic nature.

The TiO_2 nanorod assembled microflowers were prepared through a conventional hydrothermal method and HCl was used to tune their morphology (Fig. S1). Fig. 2a shows the SEM image of the TiO_2 microflowers with 1.85 mL HCl used. It could be seen that prepared TiO_2 microflowers are around 2.4 μm in diameter with a narrow size distribution. Notably, the microscale dimension of TiO_2 would facilitate the photocatalyst recycle processes through low-speed centrifuge separation (5000 rpm, 3 min). In addition, the microflower configuration could mitigate the serious loss in the surface area comparing with their solid counterparts. For the decoration of TiO_2 microflowers with BiOI nanodots, a novel reactant pre-fixing strategy was applied here to constrain the size of BiOI crystals (Fig. 2b). The reactant (BiI_3 nanodots) was pre-deposited on the surface of TiO_2 microflowers and water was subsequently added to trigger the in-situ conversion of BiI_3 to BiOI nanodots. The real content of BiOI in the as-synthesized heterostructures was investigated using TiO_2@BiOI (2%) as an example through ICP-OES. As shown in Table S1, about 0.89% of BiOI are loaded in the heterostructures when the weight ratio of BiI_3 to TiO_2 microspheres 2% was used in the synthesis process. The result was reasonable compared with the theoretical value of 1.18%, considering the loss during the synthesis process. To simplify the following discussion, the weight ratio of BiI_3 to TiO_2 microspheres instead of the real content of BiOI was used to describe the samples.

Although negligible morphology change could be observed even when up to 4% (in weight ratio of BiI_3 and TiO_2 microspheres used, same as below) BiOI nanodots were decorated (Fig. S2), the successful decoration of BiOI nanodots on the surface of TiO_2 nanorods was confirmed by the element and crystal phase analysis results. As shown in Fig. 2c, the EDS result clearly indicates the existence of Bi and I elements in the heterostructure, and the element mapping images show their homogeneous distribution in the heterostructure. Furthermore, the XRD patterns (Figs. 2d and S3) verifies that Bi and I elements were attached on the rutile-TiO_2 substrate [45] in a BiOI tetragonal [40] crystal form.
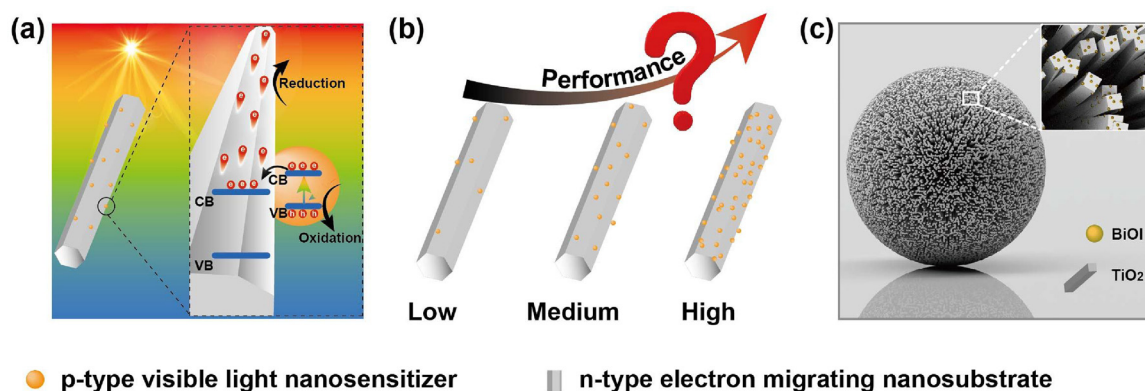

Fig. 1. (a) Schematic illustration of a general mechanism of photocatalysis process in nano-regional heterostructures upon visible light irradiation. (b) Hypothesis of the relationship between the amount of visible light sensitizers and the final photocatalytic performance. (c) Nano-regional heterostructure design mediated with TiO_2 nanorod assembled microflower and visible light sensitive BiOI nanodots.
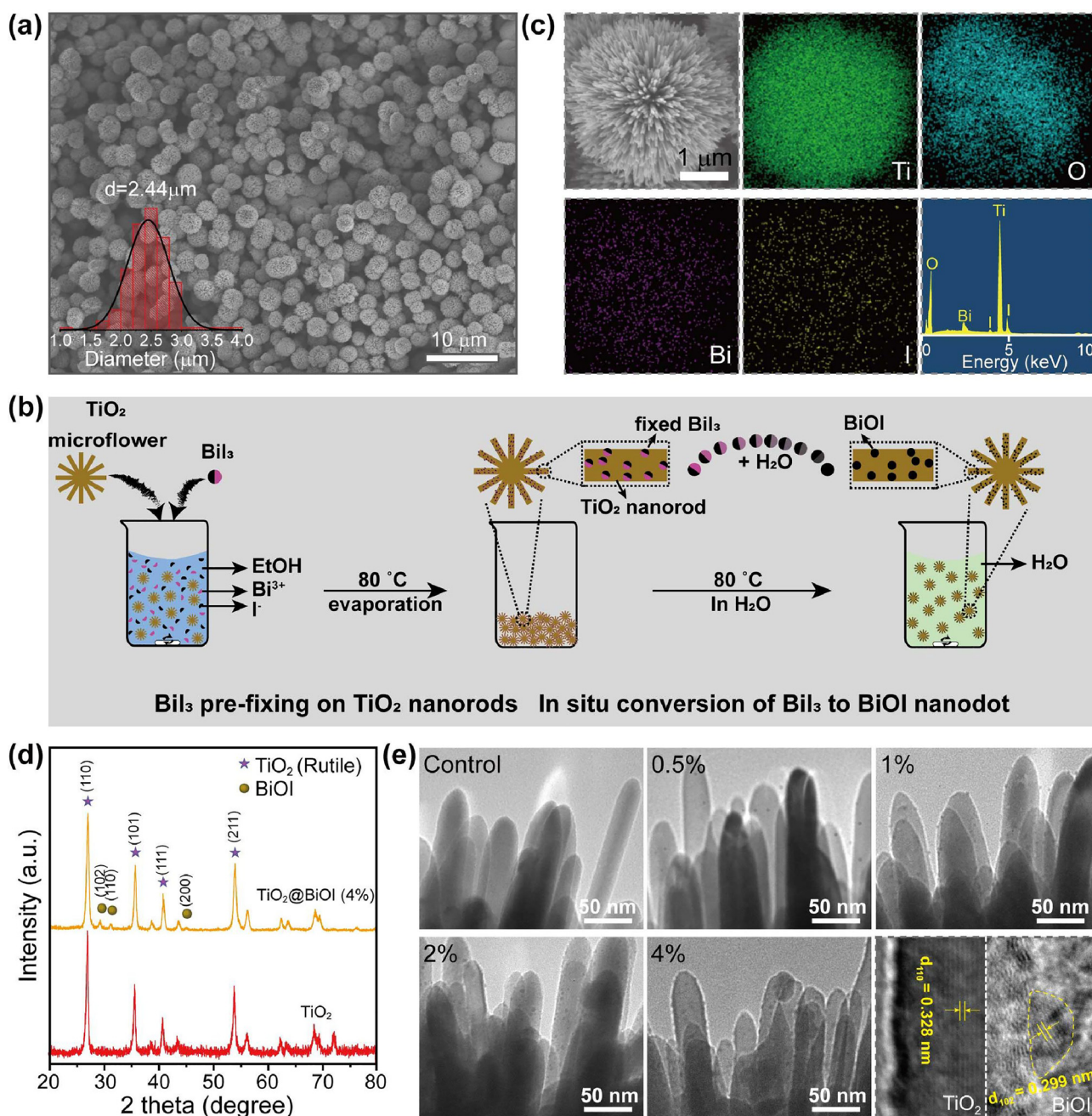
Fig. 2. (a) SEM image of the as-prepared TiO₂ nanorod assembled microflowers. (b) Schematic illustration of the reactant pre-fixing strategy for preparing ultrasmall BiOI nanodots on TiO₂ nanorods. (c) SEM image of a single TiO₂@BiOI (2%) microflower and the corresponding EDS spectra and elemental mapping images of Ti, O, Bi, and I. (d) X-ray diffraction pattern for pure TiO₂ microflowers and the TiO₂@BiOI (4%) heterostructure. (e) TEM images of TiO₂@BiOI heterostructures with varied amount of BiOI nanodots decoration. The right bottom is the high-resolution imaging of TiO₂ nanorod and BiOI nanodot.

The TEM characterization shows us the direct view of the nano-regional feature of this photocatalytic heterostructure where ultra-small BiOI nanodots were attached on the surface of bulky TiO₂ nanorods (Fig. 2e). For the control sample without BiOI decoration, smooth TiO₂ nanorods with a diameter of ~30 nm could be observed. For their modified counterparts, the existence of uniform nanodots with diameter smaller than 3 nm on the surface of TiO₂ nanorods could be easily distinguished. In addition, continuous increase in distribution density of BiOI nanodots on TiO₂ nanorods could be clearly observed when more BiI₃ was used, while the size of BiOI nanodots was almost unchanged. It should be noted that the decoration of BiOI nanodots on TiO₂ nanorods was in a random distribution manner and no nanodot clusters were found. Moreover, the clear features of crystalline lattice

obtained by high-resolution TEM revealed the high crystallinity of both TiO₂ nanorods and BiOI nanodots in the heterostructure. The BET specific surface areas of the as obtained heterostructures were tested and the result was shown in Fig. S4. A slight increase has been found along with the ascending amount of BiI₃ used during the synthesis process, indicating a continuous increase of reaction sites from TiO₂@ BiOI (0.5%) to TiO₂@BiOI (4%). Furthermore, the surface morphology, element composition and crystal phase of pure BiOI synthesized with the same method with the absence of TiO₂ microflowers were shown in Fig. S5. Without the TiO₂ microflowers as the substrate, BiOI microsheets instead of nanodots were obtained, indicating the significance of our reactant-prefixing strategy for nano-regional heterostructure preparation.
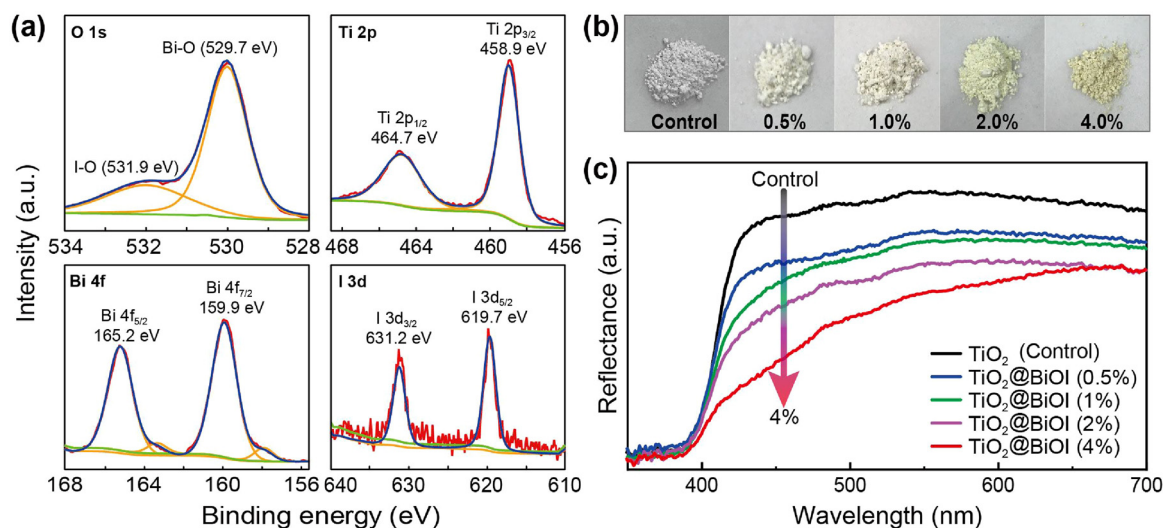
Fig. 3. (a) High-resolution XPS spectra of O 1s, Ti 2p, Bi 4f, and I 3d in the heterosturctures of TiO$_2$@BiOI (2%). (b) Photographs of TiO$_2$@BiOI heterostructures with different amounts of BiOI nanodot decorated on the surface of TiO$_2$ nanorods. (c) DRS of TiO$_2$@BiOI film samples.

To further check the chemical compositions and phase purity of BiOI and TiO$_2$ involved in these heterostructures, the surface chemical compositions and valence states of constituent elements were investigated by XPS. The corresponding signals for all the elements involved in the TiO$_2$@BiOI heterostructure can be identified in the survey spectra (Fig. S6), and the high-resolution spectra of each element are shown in Fig. 3a. In detail, the distinct peak of O 1 s at 529.7 eV corresponded to the BI—O bonds in [Bi$_2$O$_2$] slabs of BiOI layered structure [46,47], and the peak at 531.9 eV could be assigned to I—O bonds in BiOI [48,49]. The Ti 2p high-resolution XPS spectrum can be resolved into two characteristic peaks located at 458.9 eV and 464.7 eV, which can be assigned to Ti 2p$_{3/2}$ and Ti 2p$_{1/2}$ of Ti^{4+} in TiO$_2$, respectively. The characteristic peaks with bonding energies of 159.9 eV and 165.2 eV corresponding to Bi 4f$_{7/2}$ and Bi 4f$_{5/2}$ of Bi^{3+}, and two distinct peaks at 619.7 eV and 631.2 eV ascribing to I 3d$_{5/2}$ and I 3d$_{3/2}$ are assigned to I$^-$ of BiOI, [49–51] indicating the formation of BiOI in the as-prepared heterostructures. The XPS results are consistent with the reported values and agree well with the relevant information obtained from EDS (Fig. 2c), XRD (Fig. 2d), and HRTEM (Fig. 2e). Importantly, no defect states of Ti, Bi, and I were observed, evidencing the phase purity of TiO$_2$ and BiOI in these photocatalysts. Therefore, the interference from crystal defects could be ruled out from the decisive factors governing the photocatalytic processes.

Due to the visible light absorption feature of BiOI nanodots, the BiOI nanodot modified heterostructures underwent significant change in exterior color (Fig. 3b). Apparently, as the decoration amount of BiOI nanodots increased, the color of the photocatalyst changed from white to light orange and deepened gradually. To give direct evidence of the visible light responsive features of prepared photocatalytic heterostructures, their UV–vis diffuse reflection performance was studied. As shown in Fig. 3c, incident photons in the visible range beyond ~400 nm were strongly reflected by the TiO$_2$ microflowers without BiOI modification. In stark contrast, the reflectance across the whole visible-light region was significantly mitigated with increasing BiOI nanodots, indicating the strong visible light harvesting capability of our prepared nano-regional photocatalytic heterostructures.

In a further set of experiments, the photocatalytic performances of the prepared TiO$_2$@BiOI nano-regional heterostructures with varied BiOI nanodot contents were systematically evaluated by investigating their degradation capability of RhB in aqueous solution. Herein, a solar simulator was used as the light source and suitable filters were used to extract the UV and visible light, respectively. As shown in Fig. S7, RhB solution was quite stable under full spectrum solar light illumination.

Based on this prerequisite, Fig. 4a shows the variation of RhB concentration in solutions *versus* the illumination time under different light sources and with different catalysts. It can be found that, without the assistance of BiOI nanodots, TiO$_2$ microflowers could only decolorize the RhB solution by only ~37% after illuminated by the whole spectra solar light and UV light for 60 min, and almost no change could be observed when visible light was used for illumination, indicating the incapability of TiO$_2$ microspheres in visible light mediated photocatalysis. Fortunately, when the visible light sensitive BiOI nanodots were introduced, this inadequacy could be well compensated and the photodegradation rates were significantly enhanced and the optimal feed ratio of BiI$_3$ to TiO$_2$ microflowers has been proved to be 2%, regardless of the selection of irradiation light source. Especially when illuminated by full spectra solar light, a decolorization rate of ~99% was obtained using TiO$_2$@BiOI (2%) for only ~45 min, which is about 4.4 folds of that when using pure TiO$_2$ microflowers (~22.4%). In addition, the TiO$_2$@BiOI (2%) sample also showed the best photocatalytic performance under UV and visible light illumination and achieved ~97% and ~84% decolorization (after 60 min illumination), respectively. As a comparison, only about 70% of RhB could be degraded upon solar light when pure BiOI microsheets were used as the photocatalyst (Fig. S8).

GC–MS analysis of the intermediates during the RhB photodegradation process has also been conducted (Table S2) and classic intermediates like Dibutyl phthalate and Benzene acetic acid were found, as reported by the former works [52,53]. Based on this, a possible degradation pathway was proposed (Fig. S9). Besides, it has been found that after illuminated by solar light for 60 min, more than 60% of the RhB has been mineralized in the presence of TiO$_2$@BiOI (2%), as shown in Fig. S10.

The photocatalytic decolorization reaction can be described by a pseudo-first-order model, known as the Langmuir–Hinshelwood (L–H) model, which is well used in heterogeneous photocatalysis systems for low concentration of organic compounds [54]. The corresponding plots for the decolorization performances using the as-prepared photocatalysts for RhB under different light sources are shown in the inset images of Fig. 4a, which clearly indicate the first-order reaction feature of the photoinduced RhB degradation processes. Furthermore, the corresponding reaction rate constants were extracted and shown in Fig. 4b. It is obvious that the rate constants rise initially when more BiOI nanodots were involved in the heterostructure and reached a plateau at a BiOI content of 2% under all illumination conditions. However, with further increasing the decoration content of BiOI
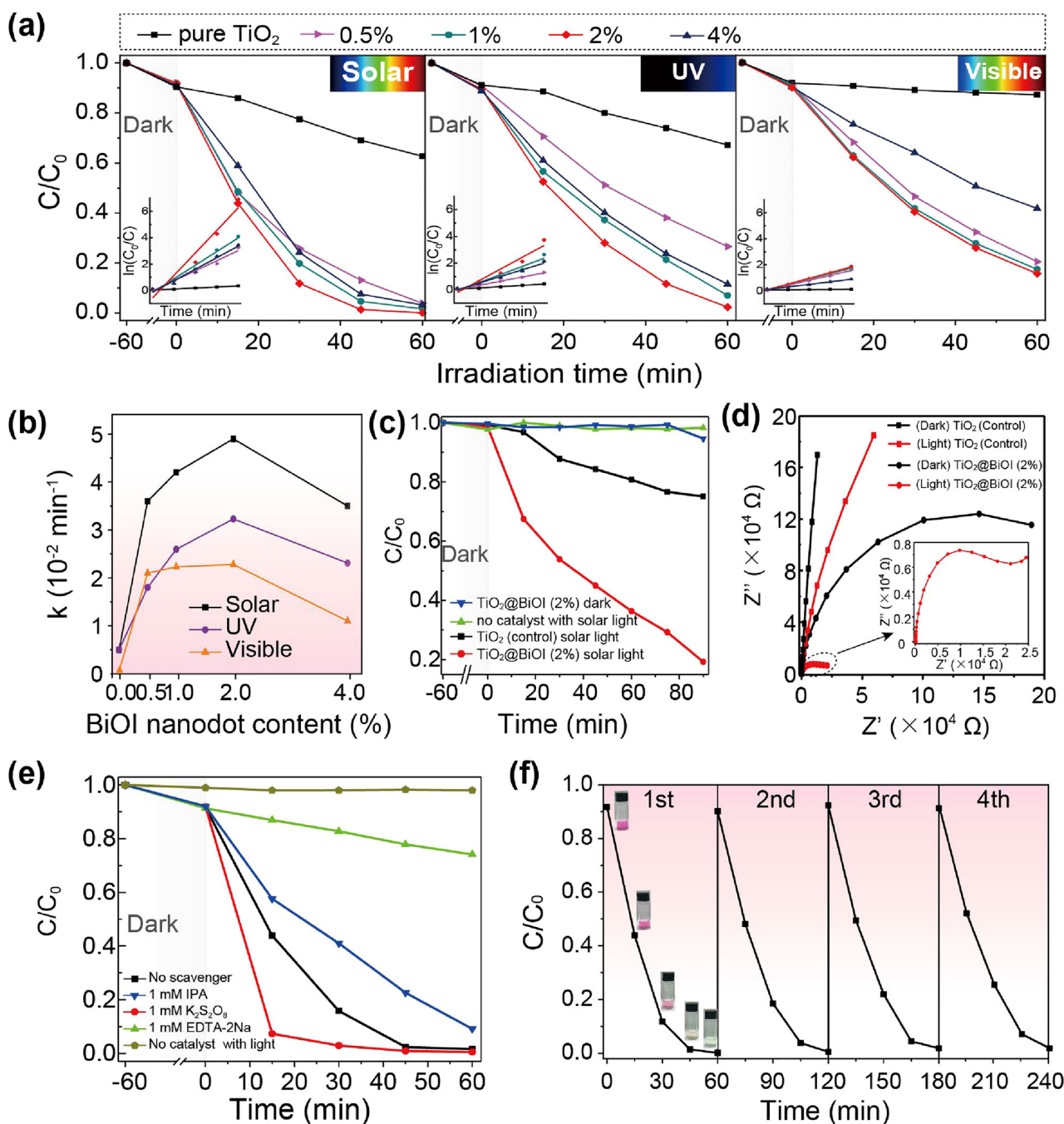
Fig. 4. (a) Rhodamine B-photodegradation performances of pure TiO₂ microflowers sample and TiO₂@BiOI heterostructures upon whole solar spectrum, UV light, and visible light illumination. Insets are the corresponding kinetic plots of $\ln(C/C_0)$ *versus* illumination time. (b) Reaction rate constants of different photocatalysts upon illumination of varied stimulation light sources. (c) Demonstration of photodegradation performances of our photocatalysts on phenol. (d) Electrochemical impedance spectroscopy for pure TiO₂ microflowers and TiO₂@BiOI (2%) with and without solar light irradiation. (e) Photocatalytic degradation performances of TiO₂@BiOI (2%) on RhB with the addition of hydroxyl radical, hole and electron scavengers. (f) Photodegradation recycle tests for TiO₂@BiOI (2%) sample upon the illumination of whole solar spectrum illumination. Inset images are the corresponding photograph of RhB solution along with the degradation timeline.

nanodots, an unexpected sharp decline of the photocatalytic rate constants was observed. For instance, upon visible light illumination for 60 min, a sample with 4% BiOI nanodot decoration (TiO₂@BiOI (4%)) could only achieve a ~58% decolorization, which is only 69% of the performance of samples with 2% BiOI decoration. Therefore, similar to the previously reported photocatalytic heterojunctions, the optimal decoration amount should be carefully controlled.

To further demonstrate the photocatalytic efficiency of our photocatalysts, colorless phenol solution was also used as target pollutant to conduct the photocatalytic process. The HPLC results in Fig. 4c showed

that more than 80% of phenol in solution could be degraded in 1.5 h in the presence of TiO₂@BiOI (2%) when illuminated by solar light, indicating the excellent photocatalytic performance of the synthesized heterostructures. As a contrast, this value was only less than 30% when TiO₂ was used as photocatalyst while almost no degradation could be observed with the absence of catalyst or light irradiation. In addition, electrochemical impedance spectroscopy (EIS) was performed to further prove the critical role of BiOI in the photocatalysts. As shown in Fig. 4d, when decorated with the optimal amount of BiOI nanodots (TiO₂@BiOI (2%)), the charge transfer resistance decreased remarkably

especially when irradiated by solar light, resulting in promoted charge transfer and enhanced photocatalytic efficiency.

In a group of additional experiments, identification of the predominant reactive species was conducted by adding corresponding reactant inhibitors in the start of the photocatalysis process. As shown in Fig. 4e, negligible degradation of RhB could be found when EDTA-2Na (hole scavenger) was added, while the capture of hydroxyl radical by IPA only caused a slight efficiency decrease. Thus, it is obvious that direct photo-excited hole oxidation mechanism mainly governs the photodegradation process [55]. Moreover, the photocatalytic efficiency was evidently promoted when $K_2S_2O_4$ was added, indicating that the redundant electrons were detrimental [56] which may cause the quenching of the effective holes.

In addition, recycle tests under full spectra solar light with TiO$_2$@BiOI (2%) were performed to evaluate the reusability of the nano-regional photocatalytic heterostructures. As shown in Fig. 4f, the adsorption ability of each cycle is nearly the same, indicating the effective reaction sites are almost not affected. After four cycles of photocatalytic tests, these photocatalysts were still able to show more than 95% photodegradation of RhB after 60 min illumination, evidencing the high durability and feasibility of our catalysts for multiple recycling photocatalysis. The XRD and XPS analysis of used photocatalysts were also conducted (Figs. S11 and S12), showing that the crystal phase remains unchanged but only a slight reduction has happened on the catalyst surface, which may be the reason of the slightly decreased photocatalytic ability.

Compared with the high photocatalytic rates and reusability of these nano-regional photocatalytic heterostructures, the counterintuitive deterioration of photocatalytic performance induced by excessive nanodot decoration draws our attention even more. In our designed nano-regional heterostructure, BiOI nanodots were used to boost the visible light harvesting ability of photocatalysts. Therefore, we can infer that more amount of BiOI nanodots on the surface of TiO$_2$ nanorods would further enhance the light absorption ability and provide more photocatalytic sites that both could motivate more efficient photocatalytic behavior. However, this prediction was clearly overturned by the aforementioned experimental results. Some researchers have suggested a possible explanation that excessive nano-decorators would lead to a light shielding effect that blocks the light absorption of other catalysts in the solution [12]. In our experiment, when 50 mg photocatalysts were dispersed in a 50 mL RhB solution, a very weak effect of light attenuation induced by the increasing the amount of BiOI nanodots could be observed. What's more, the microscale size of these microflowers could enhance the light scattering ability of the photocatalysts and result in a quasi-isotropic illumination nature. Therefore, the light shielding effect could be reasonably excluded from the main reasons for the photocatalytic performance deterioration. Some researchers also proposed that excessive nanodot decoration would cover the other photocatalytic components in the heterostructure and then lead to the loss of effective photocatalytic sites [31]. Quite differently, in our situation, the photocatalytic sites are located in the BiOI nanodots instead of TiO$_2$ nanorods. On the premise of this, more BiOI nanodot decoration would theoretically increase the number of effective photocatalytic sites, instead of blocking them. Therefore, we can infer that, in a typical nano-regional photocatalytic heterostructure, there must exist some other overlooked channels that may play an important role in deteriorating their overall photocatalytic performance.

Let us revisit the working mechanism of the TiO$_2$@BiOI mediated heterostructure in photodegradation (Fig. 5a). Upon visible light illumination, benefiting from the ultrasmall physical dimension of BiOI nanodots (< 3 nm), photoinduced electrons can diffuse quickly to their surface in only a few migration steps. Thus, we can expect a much higher exciton separation efficiency in BiOI nanodots comparing with that of conventionally used nano or even microcrystals which suffer severe electron-hole recombination during the exciton diffusion in their crystal lattice. Furthermore, with holes left in the valence band,

electrons in the conduction band of BiOI nanodots can drift across the p-n junction and diffuse freely along the bulky TiO$_2$ nanorods, resulting in long-lasting charge separation, which is a key factor for the design of a high- performance photocatalysts [57–60]. However, besides the intrinsic excitons' recombination within BiOI (Fig. 5a, stage 1), it is notable that electrons migrating along the TiO$_2$ nanorods are not absolutely free since those electrons from one BiOI nanodot would have a certain probability of encountering other nanodots during their diffusion processes and being captured by holes exposed in the valence band of the latter (Fig. 5a, stage 2). Thus, the recombination between electrons in TiO$_2$ nanorods and holes in BiOI nanodots could be a possible channel of losing effective photocatalytic sites. Importantly, this photocatalytic site quenching effect would aggravate rapidly when more BiOI nanodots were decorated on the surface of TiO$_2$ nanorods (Fig. 5b). Finally, after exceeding a certain decoration amount, this detrimental effect would win the competition with other positive effects (such as enhanced light harvesting ability and increased reaction sites), resulting in serious photocatalytic performance decline. Here we proposed a mechanism called "photocatalytic site self-quenching" to provide an accurate expression of this effect since the loss of effective catalytic sites on BiOI nanodots is induced by electrons generated from themselves under visible light illumination. It should be mentioned that the photoinduced interfacial charge carrier recombination is a widely accepted recombination pathway for dye-sensitized solar cells [61–63] and perovskite solar cells [64,65], and this electron-backflow recombination could severely reduce the charge separation efficiency and consequently the overall photoelectric energy conversion efficiency. Similarly, we believe the photocatalytic site self-quenching effect in nano-regional heterostructures could also be a crucial pathway diminishing the overall photocatalytic performance.

To provide solid evidence of the photocatalytic site self-quenching effect proposed above, kinetic processes of photoinduced excitons in the heterostructure was further investigated. Here, upon 420 nm pulse laser excitation (only BiOI were excited), the photoinduced fluorescence decay (λ_{em} = 550 nm) curves of the TiO$_2$@BiOI heterostructures were recorded (Fig. 5c). It is quite clear that all the fluorescence decay curves from the heterostructures with various BiOI contents follow the double-exponential decay mode, which contains a faster (stage 1) and a much slower (stage 2) decay stages. Thus, we can reasonably infer that the depopulation process of photoinduced electrons in BiOI nanodots is governed by two major pathways with very different recombination rates. In addition, as indicated by the turning curve, the time required for transition from stage 1 to stage 2 was obviously shortened with more BiOI nanodots decorated. Concomitantly, the contribution from stage 1 to the fluorescence gradually decreased, on the contrary, that from stage 2 increased accordingly. More importantly, for stage 2, the decay rate was much lower than that of stage 1, this is because electrons from the conduction band of BiOI nanodots need to migrate for a certain distance along TiO$_2$ nanorods before they are trapped by adjacent BiOI nanodots. Thereby, with more BiOI content on TiO$_2$, the distance between BiOI nanodots could be reduced significantly and the time required for electrons migrating along TiO$_2$ nanorods to meet the surrounding BiOI nanodots could be shortened, resulting in the early appearance of the stage 2. This explanation could be strongly proven by the significantly reduced fluorescence lifetime governed by stage 2. In heterostructures with higher distribution density of BiOI nanodots, the recombination rate of electrons migrating along TiO$_2$ nanorods with certain BiOI nanodots would be much higher, thus leading to shortened fluorescence lifetime (stage 2). However, the high-density decoration of BiOI nanodots would show negligible effect on the depopulation process of electrons within BiOI nanodots themselves, which is also evidenced by the very slight change in lifetime of stage 1. Therefore, with TiO$_2$@BiOI mediated heterostructure as a typical example, the existence and crucial role of photocatalytic site self-quenching effect in nano-regional photocatalytic heterostructure was proved.
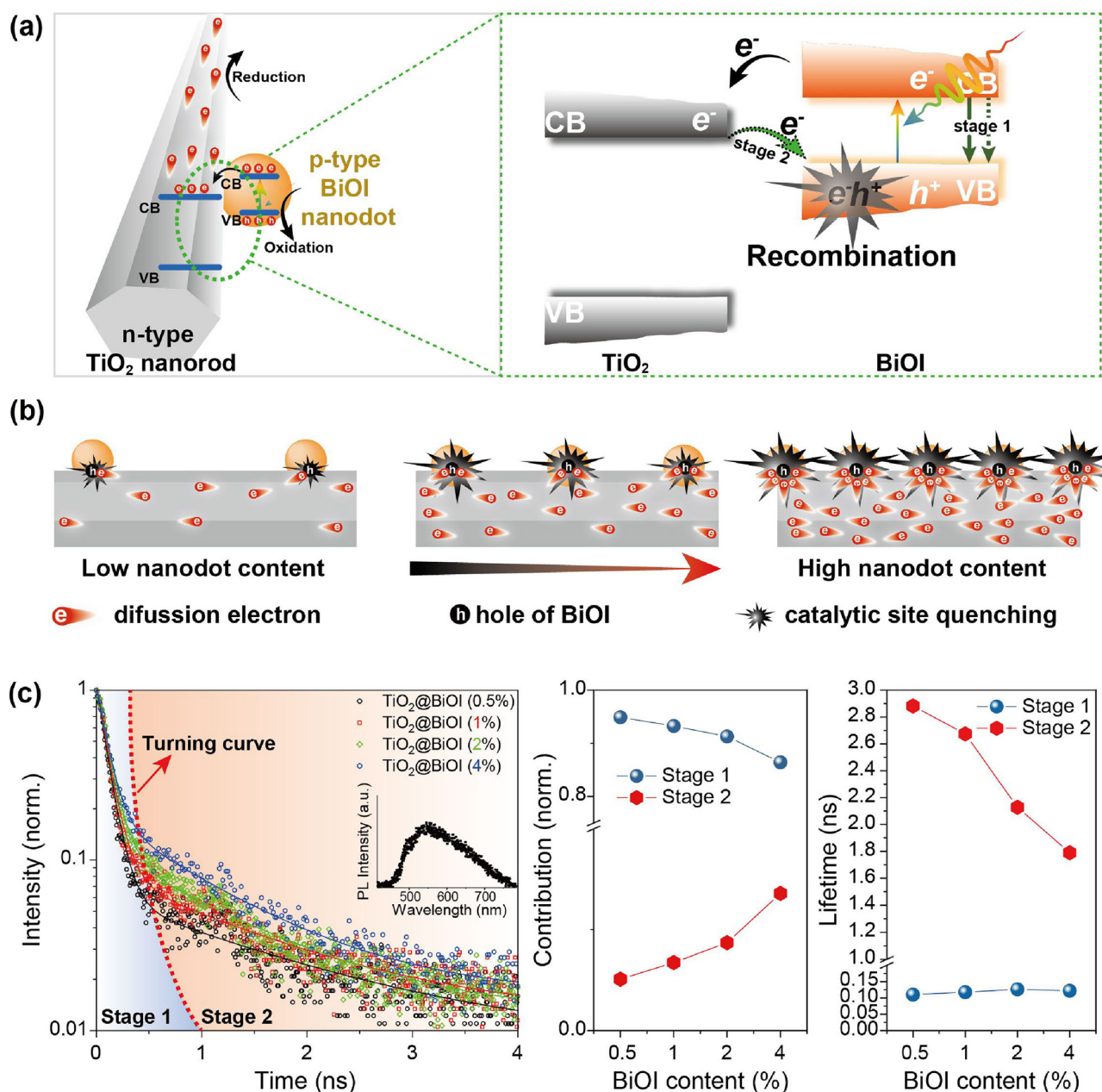
Fig. 5. (a) Schematic illustration of the two recombination stages of photoinduced electrons upon visible light illumination: stage 1, the recombination within BiOI; stage 2, the recombination between electrons already transported to TiO₂ and holes exposed in BiOI. (b) The photocatalytic site self-quenching processes in nano-regional photocatalytic heterostructure with different amounts of nano-decorators. (c) Left, Fluorescence decay curves of nanostructures with different BiOI contents. Inset is the photoluminescence of TiO_2@BiOI (4%) upon 420 nm excitation. Middle, Fluorescence contribution of stage 1 and 2 extracted from fluorescence decay curves. Right, lifetime variation of stage 1 and 2 with increased BiOI nanodot content.

4. Conclusions

In this work, we proposed a possible recombination pathway of "photocatalytic site self-quenching" for photoinduced excitons in nano-regional photocatalytic heterostructures. To prove the crucial role of this effect, a classical p-n heterojunction composed of n-type TiO_2 nanorod assembled microflowers and p-type BiOI nanodots with varied contents were synthesized, and RhB was used as a conventional signal to probe the photocatalytic performances of the designed heterostructures. It has been found that along with the increasing content of BiOI nanodots in the heterostructure, the photocatalytic efficiency showed first increase and then decrease with an optimal BiOI content of 2%. This parabolic variation may stem from the gambling between enhanced number of reaction sites and aggravated photocatalytic cite

self-quenching effect where the photocatalytic sites on BiOI nanodots would be quenched by electrons migrating along TiO_2 nanorods. This proposed mechanism was further verified by the time-resolved fluorescence decay curve, indicating that the increased distribution density of BiOI nanodots on the surface of TiO_2 nanorods could shorten the migrating time of BiOI generated electrons along TiO_2 nanorods and increase their probability to recombine with adjacent BiOI nanodots. Our study proposed the photocatalytic reaction sites self-quenching effect which has long been overlooked in the heterostructure based photocatalytic field and exemplified it using a classical nano-regional heterostructure. It is expected that this work could offer guidance for the rational design of high-performance functional heterostructures in the field of photocatalysis or even photovoltaics field.

Author contributions

H.F. conceived the idea. H.F. and Liang.L. designed the experiments. Lin.L., Z.H., and Y.L. supervised the research. Liang.L carried out the synthesis of the photocatalyst and H.F. did the basic characterization, and testing of the photocatalytic abilities of different catalysts. The paper was primarily written by H. F. and Liang. L., and all authors contributed to the editing of the manuscript.

Competing financial interest

The authors declare no competing financial interest.

Acknowledgments

References

[1] Y.-L. Lee, Y.-S. Lo, Adv. Funct. Mater. 19 (2009) 604–609.
[2] L. Liang, Y. Liu, X.-Z. Zhao, Chem. Commun. 49 (2013) 3958–3960.
[3] H.-S. Kim, J.-W. Lee, N. Yantara, P.P. Boix, S.A. Kulkarni, S. Mhaisalkar, M. Grätzel, N.-G. Park, Nano Lett. 13 (2013) 2412–2417.
[4] V. Andreev, Semiconductors 33 (1999) 942–945.
[5] L. Liang, Y. Liu, C. Bu, K. Guo, W. Sun, N. Huang, T. Peng, B. Sebo, M. Pan, W. Liu, Adv. Mater. 25 (2013) 2174–2180.
[6] M. Tucci, G. De Cesare, J. Non-Cryst. Solids 338 (2004) 663–667.
[7] Y. Hu, T. Qiu, F. Bai, W. Ruan, S. Zhang, Adv. Energy Mater. (2018) 1703620.
[8] X. An, F. Liu, Y.J. Jung, S. Kar, Nano Lett. 13 (2013) 909–916.
[9] W. Tian, T. Zhai, C. Zhang, S.L. Li, X. Wang, F. Liu, D. Liu, X. Cai, K. Tsukagoshi, D. Golberg, Adv. Mater. 25 (2013) 4625–4630.
[10] C. Xie, B. Nie, L. Zeng, F.-X. Liang, M.-Z. Wang, L. Luo, M. Feng, Y. Yu, C.-Y. Wu, Y. Wu, ACS Nano 8 (2014) 4015–4022.
[11] J. Zhang, F.-X. Xiao, G. Xiao, B. Liu, Appl. Catal. A: Gen. 521 (2016) 50–56.
[12] M. Zhou, S. Wang, P. Yang, C. Huang, X. Wang, ACS Catal. (2018) 4928–4936.
[13] L. Zhu, H. Li, Z. Liu, P. Xia, Y. Xie, D. Xiong, J. Phys. Chem. C 122 (2018) 9531–9539.
[14] F.-X. Xiao, J. Miao, B. Liu, J. Am. Chem. Soc. 136 (2014) 1559–1569.
[15] Z. Guo, B. Liu, Q. Zhang, W. Deng, Y. Wang, Y. Yang, Chem. Soc. Rev. 43 (2014) 3480–3524.
[16] M. Ge, Q. Li, C. Cao, J. Huang, S. Li, S. Zhang, Z. Chen, K. Zhang, S.S. Al-Deyab, Y. Lai, Adv. Sci. 4 (2017) 1600152.
[17] X. Yu, J. Liu, A. Genc, M. Ibanez, Z. Luo, A. Shavel, J. Arbiol, G. Zhang, Y. Zhang, A. Cabot, Langmuir 31 (2015) 10555–10561.
[18] K. Li, B. Peng, T. Peng, ACS Catal. 6 (2016) 7485–7527.
[19] K. Sekizawa, S. Sato, T. Arai, T. Morikawa, ACS Catal. 8 (2018) 1405–1416.
[20] G. Li, L. Wu, F. Li, P. Xu, D. Zhang, H. Li, Nanoscale 5 (2013) 2118–2125.
[21] Y. Ao, J. Bao, P. Wang, C. Wang, J. Hou, Dalton Trans. 45 (2016) 13907–13916.
[22] Z. He, Y. Shi, C. Gao, L. Wen, J. Chen, S. Song, J. Phys. Chem. C 118 (2014) 389–398.
[23] Z. Duan, G. Henkelman, ACS Catal. (2018) 1376–1383.
[24] Y. Hou, Y. Liu, R. Gao, Q. Li, H. Guo, A. Goswami, R. Zboril, M.B. Gawande, X. Zou, ACS Catal. (2017) 7038–7042.
[25] L. Dandan, Y. Shu-Hong, J. Hai-Long, Adv. Mater. 0 (2018) 1707377.
[26] Y. Sang, Z. Zhao, M. Zhao, P. Hao, Y. Leng, H. Liu, Adv. Mater. 27 (2015) 363–369.
[27] S.S. Gujral, A.N. Simonov, M. Higashi, X.-Y. Fang, R. Abe, L. Spiccia, ACS Catal. 6 (2016) 3404–3417.
[28] S. Sun, H. Liu, L. Wu, C.E. Png, P. Bai, ACS Catal. 4 (2014) 4269–4276.
[29] J.-C. Wang, H.-C. Yao, Z.-Y. Fan, L. Zhang, J.-S. Wang, S.-Q. Zang, Z.-J. Li, ACS Appl. Mater. Interfaces 8 (2016) 3765–3775.
[30] D. Sarkar, C.K. Ghosh, S. Mukherjee, K.K. Chattopadhyay, ACS Appl. Mater. Interfaces 5 (2013) 331–337.
[31] M.Y. Ye, Z.H. Zhao, Z.F. Hu, L.Q. Liu, H.M. Ji, Z.R. Shen, T.Y. Ma, Angew. Chem. (2017).
[32] J. Di, J. Xia, M. Ji, B. Wang, S. Yin, H. Xu, Z. Chen, H. Li, Langmuir 32 (2016) 2075–2084.
[33] H. Xu, Y. Xu, H. Li, J. Xia, J. Xiong, S. Yin, C. Huang, H. Wan, Dalton Trans. 41 (2012) 3387–3394.
[34] A.-W. Xu, Y. Gao, H.-Q. Liu, J. Catal. 207 (2002) 151–157.
[35] S.S. Lo, T. Mirkovic, C.H. Chuang, C. Burda, G.D. Scholes, Adv. Mater. 23 (2011) 180–197.
[36] D. Chen, J. Yang, Y. Zhu, Y. Zhang, Y. Zhu, Appl. Catal. B: Environ. 233 (2018) 202–212.
[37] J. Cao, B. Xu, H. Lin, B. Luo, S. Chen, Dalton Trans. 41 (2012) 11482–11490.
[38] H. Cheng, B. Huang, Y. Dai, Nanoscale 6 (2014) 2009–2026.
[39] H. Huang, X. Han, X. Li, S. Wang, P.K. Chu, Y. Zhang, ACS Appl. Mater. Interfaces 7 (2015) 482–492.
[40] L. Sun, L. Xiang, X. Zhao, C.-J. Jia, J. Yang, Z. Jin, X. Cheng, W. Fan, ACS Catal. 5 (2015) 3540–3551.
[41] X.-J. Wen, C.-G. Niu, L. Zhang, G.-M. Zeng, ACS Sustain. Chem. Eng. (2017).
[42] D. Sarkar, C.K. Ghosh, K.K. Chattopadhyay, CrystEngComm 14 (2012) 2683–2690.
[43] Z. Zhu, H. Pan, M. Murugananthan, J. Gong, Y. Zhang, Appl. Catal. B: Environ. 232 (2018) 19–25.
[44] Y. Lai, M. Meng, Y. Yu, Appl. Catal. B: Environ. 100 (2010) 491–501.
[45] B. Liu, E.S. Aydil, J. Am. Chem. Soc. 131 (2009) 3985–3990.
[46] J. Liu, L. Ruan, S.B. Adeloju, Y. Wu, Dalton Trans. 43 (2014) 1706–1715.
[47] G. Dai, J. Yu, G. Liu, J. Phys. Chem. C 115 (2011) 7339–7346.
[48] C. Yu, J.C. Yu, C. Fan, H. Wen, S. Hu, Mater. Sci. Eng. B 166 (2010) 213–219.
[49] C. Chang, L. Zhu, S. Wang, X. Chu, L. Yue, ACS Appl. Mater. Interfaces 6 (2014) 5083–5093.
[50] J. Di, J. Xia, Y. Ge, L. Xu, H. Xu, J. Chen, M. He, H. Li, Dalton Trans. 43 (2014) 15429–15438.
[51] H. Liu, W. Cao, Y. Su, Y. Wang, X. Wang, Appl. Catal. B: Environ. 111 (2012) 271–279.
[52] X. Miao, X. Yue, X. Shen, Z. Ji, H. Zhou, G. Zhu, J. Wang, L. Kong, M. Liu, C. Song, Catal. Sci. Technol. 8 (2018) 632–641.
[53] Z. He, S. Yang, Y. Ju, C. Sun, J. Environ. Sci. 21 (2009) 268–272.
[54] D. Sarkar, U. Maiti, C. Ghosh, K. Chattopadhyay, Adv. Sci. Lett. 6 (2012) 127–133.
[55] T. Xu, L. Zhang, H. Cheng, Y. Zhu, Appl. Catal. B: Environ. 101 (2011) 382–387.
[56] A. Syoufian, K. Nakashima, J. Colloid Interface Sci. 313 (2007) 213–218.
[57] K. Wu, H. Zhu, Z. Liu, W. Rodríguez-Córdoba, T. Lian, J. Am. Chem. Soc. 134 (2012) 10337–10340.
[58] M. Zhang, X. Wang, Energy Environ. Sci. 7 (2014) 1902–1906.
[59] J. Zhang, M. Zhang, C. Yang, X. Wang, Adv. Mater. 26 (2014) 4121–4126.
[60] J. Li, L. Cai, J. Shang, Y. Yu, L. Zhang, Adv. Mater. 28 (2016) 4059–4064.
[61] M. Wang, C. Grätzel, S.M. Zakeeruddin, M. Grätzel, Energy Environ. Sci. 5 (2012) 9394–9405.
[62] S. Zhang, X. Yang, C. Qin, Y. Numata, L. Han, J. Mater. Chem. A 2 (2014) 5167–5177.
[63] S. Handa, H. Wietasch, M. Thelakkat, J.R. Durrant, S.A. Haque, Chem. Commun. (2007) 1725–1727.
[64] Q. Shen, Y. Ogomi, J. Chang, T. Toyoda, K. Fujiwara, K. Yoshino, K. Sato, K. Yamazaki, M. Akimoto, Y. Kuga, J. Mater. Chem. A 3 (2015) 9308–9316.
[65] M.I. Dar, M. Franckevičius, N. Arora, K. Redeckas, M. Vengris, V. Gulbinas, S.M. Zakeeruddin, M. Grätzel, Chem. Phys. Lett. 683 (2017) 211–215.